

Modeling the Influence of Upstream Land–Atmosphere Coupling on the 2017 Persistent Drought over Northeast China^❶

DINGWEN ZENG^{a,b,c} AND XING YUAN^{a,b}

^a School of Hydrology and Water Resources, Nanjing University of Information Science and Technology, Nanjing, China

^b Key Laboratory of Regional Climate-Environment for Temperate East Asia, Institute of Atmospheric Physics, Chinese Academy of Sciences, Beijing, China

^c Key Laboratory of Arid Climatic Change and Reducing Disaster of Gansu Province, and Key Open Laboratory of Arid Climate Change and Disaster Reduction, Institute of Arid Meteorology, China Meteorological Administration, Lanzhou, China

(Manuscript received 16 August 2020, in final form 1 February 2021)

ABSTRACT: Persistent drought events that cause serious damage to the economy and environment are usually intensified by the feedback between the land surface and atmosphere. Therefore, reasonably modeling land–atmosphere coupling is critical for skillful prediction of persistent droughts. However, most high-resolution regional climate modeling has focused on the amplification effect of land–atmosphere coupling on local anticyclonic circulation anomalies, while less attention has been paid to the nonlocal influence through altering large-scale atmospheric circulation. Here we investigate how the antecedent land–atmosphere coupling over the area south of Lake Baikal (ASLB) influences the drought events occurring over its downstream region [i.e., Northeast China (NEC)] by using the Weather Research and Forecasting (WRF) Model and a linear baroclinic model (LBM). When the ASLB region is artificially forced to be wet in the WRF simulations during March–May, the surface sensible heating is weakened and results in a cooling anomaly in low level atmosphere during May–July. Consequently, the anticyclonic circulation anomalies over ASLB and NEC are weakened, and the severity of NEC drought during May–July cannot be captured due to the upstream wetting in March–May. In the LBM experiments, idealized atmospheric heating anomaly that mimics the diabatic heating associated with surface wetness is imposed over ASLB, and the quasi-steady response pattern of 500-hPa geopotential height to the upstream wetting is highly consistent with that in the WRF simulation. In addition, the lower-level heating instead of the upper-level cooling makes a major contribution to the high pressure anomaly over NEC. This study implies the critical role of modeling upstream land–atmosphere coupling in capturing downstream persistent droughts.

KEYWORDS: Drought; Atmosphere-land interaction; Sensible heating; Soil moisture; Regional models; Climate variability

1. Introduction

Droughts over East Asia have become an increasing concern in recent years, and have caused compounding ecosystem and societal stresses because of persistently below-normal precipitation. With global warming, both the frequency and duration of droughts show an increasing trend (Zhai et al. 2010; Zhang and Zhou 2015). Northeast China (NEC) is an important grain depot, but it has frequently suffered from severe drought events in recent decades (Yu et al. 2014; Han et al. 2015; Wang and He 2015; S. Wang et al. 2019). This raises an urgent need to unravel underlying processes and mechanisms, especially those relevant to drought early warning (Yuan and Wood 2013).

NEC is located in the northernmost part of East Asian monsoon region, and its summer precipitation is influenced by the external forcings from both the tropics and the middle to high latitudes. El Niño–Southern Oscillation (ENSO) is considered as a principal factor affecting precipitation anomaly over NEC (Sun and Wang 2006). The relationship between spring

eastern ENSO and summer rainfall over NEC has been enhanced since 2000, and thus a lower Niño-3 index might correspond to less NEC precipitation, with the tropical Indian Ocean acting as a bridge to link them (Han et al. 2017). ENSO can also modulate abnormal moisture transportation patterns related to the NEC drought (X. Li et al. 2015). At middle and high latitudes, the loss of sea ice over the Barents Sea in spring may lead to NEC drought during July–August, through increasing the snow depth over western Eurasia and triggering the associated polar–Eurasia teleconnection pattern (Li et al. 2018; S. Wang et al. 2019). The intense warming over the European continent and Caspian Sea in spring can strengthen the anticyclonic circulation anomaly over the Tibetan Plateau, and may result in the NEC drought during July–August (Wang and He 2015). The negative phase of summer North Atlantic Oscillation can also lead to a NEC drought event (Sun and Wang 2012).

Besides the remote influences mentioned above exerted by the ocean and sea ice through Rossby waves (Schubert et al. 2011, 2014), the local feedback between soil moisture and atmospheric boundary layer also makes a significant contribution to the maintenance of drought, which intensifies the local anticyclonic circulation anomaly through transporting massive surface sensible heating into atmosphere. During the 2010 Russian heat wave and the 2003 European heat wave events (Fischer et al. 2007a; Dole et al. 2011; Lau and Kim 2012), the sensible heat flux had a strong maintenance and amplification

^❶ Supplemental information related to this paper is available at the Journals Online website: <https://doi.org/10.1175/JCLI-D-20-0650.s1>.

Corresponding author: Xing Yuan, xyuan@nuist.edu.cn

effect on the local positive anomalies of geopotential height, and ultimately resulted in severe droughts. The associated feedback processes are regarded as follows: once the below-normal precipitation induces a negative soil moisture anomaly, the anomaly of land-atmosphere coupling will be initiated and it potentially sustains a long-lasting (from weeks to months) soil moisture deficit (Roundy et al. 2013; Entin et al. 2000). The persistently strong sensible heat flux may heat the low-level atmosphere and lead to extremely high temperature (Miralles et al. 2014; Hirschi et al. 2011), and reduce the evapotranspiration and atmospheric water vapor content. Conversely, the increased atmospheric vapor pressure deficit can exacerbate the soil moisture depletion (Teuling et al. 2013; Zhou et al. 2019). Together with the vapor dissipation due to the large-scale divergent circulation, such positive land-atmosphere feedback sustains the dry conditions of both land and atmosphere, and the heat accumulation strongly modulates the large-scale anomalous anticyclone (Fischer et al. 2007b; Zeng et al. 2019).

The above local feedbacks between land and atmosphere were also verified in coupled regional climate simulations. High-resolution regional simulations can well capture the temporal variability and spatial pattern of drought events (Diasso and Abiodun 2017), and suggest that the memory of the surface dryness is a necessary sources of drought predictability (PaiMazumder and Done 2016).

Besides the local feedback, land-atmosphere coupling also has a nonlocal effect on atmospheric circulation through changing the thermal and dynamical processes in the atmosphere (Duerinck et al. 2016; Xue et al. 2016; Schumacher et al. 2019). On the one hand, the soil moisture anomaly can change the atmospheric baroclinicity at low levels, and thus the changed thermal difference in latitudinal and meridional directions alters the large-scale circulation. For example, anomalous wet soil over West Africa will lead to surface evaporative cooling, and then the modified meridional temperature gradients result in poleward movement of the midlevel African easterly jet, and finally enhance the precipitation (Berg et al. 2017). Across the Yangtze River valley to the North China region, anomalous wet soil in late spring may reduce the land-sea thermal contrast during summer, resulting in the weakened East Asian summer monsoon (Zhang and Zuo 2011). On the other hand, the soil moisture and temperature anomalies lasting for a long period may act as a forcing source of the Rossby wave in westerlies. Warm springtime surface soil temperature in high-altitude areas (e.g., the western United States and the Tibetan Plateau) can trigger stationary waves with a local anticyclonic circulation anomaly located over the plateau area and a cyclone located over the downstream plain regions (Xue et al. 2012, 2018). For the extreme drought event that occurred over the Great Plains of North America in 2012, if an artificial soil dryness is imposed over target regions in the GCM model, a high anomaly will be excited in western North America, and a low anomaly will be formed over eastern North America due to eastward energy dispersion (Koster et al. 2016), which can be considered as a phase-blocking effect of the dry surface on the atmosphere. Further simulations with a stationary wave model show that the phase blocking is

closely related to the base flow (climate mean state of circulation) and the local orography (H. Wang et al. 2019). A linear baroclinic model (LBM) was also used to study the contribution of tropical circulation to the central American midsummer drought (Small et al. 2007). However, the non-local effects of land-atmosphere coupling during extreme drought events have largely been ignored in middle to high latitudes of East Asia. Zeng et al. (2019) speculated that the anticyclonic anomaly located over the upstream regions [area south of Lake Baikal (ASLB)] was the direct cause during the persistency of the NEC drought, and further analysis indicated that the sensible heating due to land-atmosphere coupling over the ASLB region was a key factor for maintaining this local anticyclonic anomaly (Zeng et al. 2019). While this conclusion is based on diagnostic analysis by using reanalysis data, it is difficult to well isolate land-atmosphere coupling from the thermal forcings due to other factors (e.g., ocean, atmospheric internal variability, etc.). In this study, we aim to answer the following two questions through a series of numerical experiments: 1) Based on a high-resolution regional climate modeling, can the antecedent land-atmosphere coupling over ASLB intensify the consequent drought event occurring over downstream region (NEC) through altering atmospheric circulation? 2) Can the above thermodynamic processes be verified by the simplified modeling (e.g., LBM)?

This paper is arranged as follows: the reanalysis data, numerical models [the Weather Research and Forecasting (WRF) Model and the LBM], and experimental design are described in section 2. In section 3a, convective parameterization schemes in the WRF Model are tested to better simulate the NEC drought event of 2017, and then the long-term control experiment is conducted. In section 3b, the result of sensitivity experiment is analyzed, in which an artificial surface thermal anomaly is imposed in the target regions. In section 3c, we force the LBM with idealized heating anomalies and verify the proposed drought mechanism, where the anomalous heating profiles can mimic the diabatic heating and cooling effect of surface soil on the low-level atmosphere, which correspond to the profiles in the control and sensitivity experiments, respectively, conducted by the WRF Model. A summary and discussion of this study are provided in section 4.

2. Datasets, models, and experimental design

a. Data

Pressure-level atmospheric data and 0–100-cm soil moisture data from 1981 to 2017 are derived from the ERA-Interim reanalysis (Dee et al. 2011). The 6-hourly ERA-Interim atmospheric and oceanic datasets with 0.75° spatial resolution and 37 vertical pressure levels are also used to force the WRF Model. The ERA-Interim geopotential height, atmospheric temperature, meridional and zonal wind velocity, and relative humidity at the pressure levels and SST provide boundary and initial conditions for the WRF simulations, where the boundary conditions are updated every 6 h. ERA-Interim sea ice cover, snow density and depth, soil temperature and moisture at four soil levels, and skin temperature are used to provide

TABLE 1. Model configuration and physical schemes.

Model configuration and physical schemes	
Domain center	36°N, 110°E
Horizontal resolution	30 km
Horizontal grid cells	250 × 197
Vertical layers	30
Radiation physics	RRTMG (Iacono et al. 2008)
Microphysics	WSM3 (Hong et al. 2006b)
Cumulus physics	Kain–Fritsch (Kain 2004)
PBL physics	YSU (Hong et al. 2006a)
Land surface model	Noah (Chen et al. 1996)

initial conditions for the WRF simulations. Monthly gridded precipitation data at 1.0° resolution obtained from NOAA's Precipitation Reconstruction (PREC) data are used as observation (Chen et al. 2002).

b. WRF Model and experimental design

The Advanced Research version of WRF, version 3.8.1, is applied to explore how land–atmosphere coupling influences the NEC drought through altering atmospheric circulation in this study. WRF is a nonhydrostatic and fully compressible model, which is widely used for forecasting and research at seasonal time scales as well as for land–atmosphere coupling research during drought and heat wave events (Yuan et al. 2012; Zaitchik et al. 2013; Powers et al. 2017; Li et al. 2018). The model configuration and physical schemes used in this study are listed in Table 1 and the model domain is shown in Fig. 1. The WRF experimental setting is summarized briefly in Table 2, where we conduct climatological seasonal simulations (CLIM) covering the period from 1981 to 2010, and the simulations for each year begin from 25 February and end on 31 July. For 2017, we conduct a control simulation (CTL) and two sensitivity simulations (SENS1 and SENS2) that also begin from 25 February and end on 31 July. For all simulations, the results during March–July are used, while the results during February are regarded as model spinup and are dropped (Table 2). When the WRF Model is used to conduct the seasonal-scale regional climate modeling, the spinup time is usually 4–9 days (Gochis et al. 2002; Zhong et al. 2007; Yuan et al. 2012; Wang et al. 2014; W. Li et al. 2015). This is reasonable to make use of the memory of the initial soil moisture anomaly that lasts for a few months (Liang and Yuan 2021). In fact, the operational seasonal forecasting usually neglects the spinup to fully assimilate the information from initial oceanic and land surface anomalies (Saha et al. 2014). This can be achieved through comprehensive data assimilation to approach the realistic initial conditions, and the reanalysis data that assimilate multisource observations are usually used to provide initial conditions for seasonal forecasts or simulations. In this study, we use the ERA-Interim reanalysis to provide initial conditions and regard the first 5 days as the spinup, which is reasonable for CLIM and CTL experiments. For the SENS1 and SENS2 experiments, it is complicated to consider the spinup because we reset the precipitation or soil moisture every day, so the system cannot fully reach the balance. But we

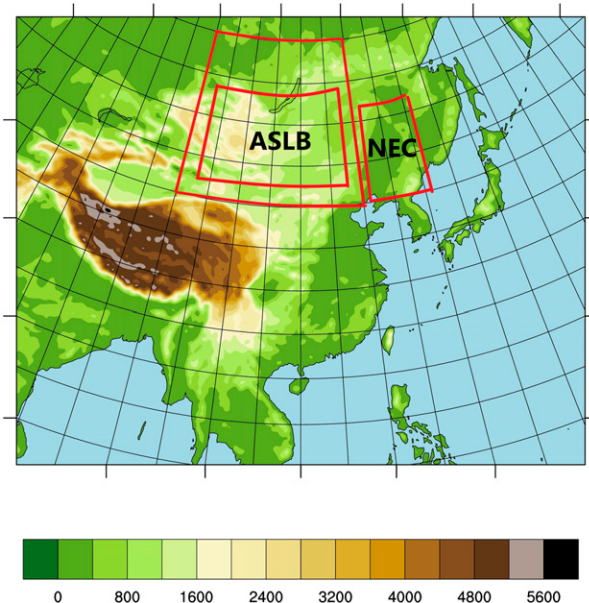


FIG. 1. WRF Model domain and the topography height (shaded; m). The area marked by the biggest red box was forced to be wet during March–May of 2017 in the WRF sensitivity simulations, and Northeast China (NEC) and the area south of Lake Baikal (ASLB) were marked by small red boxes.

speculate that the strong forcing from the land surface anomaly can outweigh the chaos brought by the imbalance, and the influence of the imbalance should be limited. Quantifying the impact of the “spinup imbalance” is beyond the scope of this study, although it might be an interesting topic if a more appropriate experiment could be designed.

Our previous diagnosis showed that drought events occurred concurrently over NEC and ASLB in 2017, and suggested that the NEC drought resulted from the anticyclonic circulation anomaly over ASLB, where the land–atmosphere coupling induced sensible heating over ASLB is the maintain factor of this anticyclonic circulation anomaly (Zeng et al. 2019). So an artificial wetness is imposed over ASLB to weaken or eliminate the surface heating effect in the two sensitivity experiments respectively (SENS1 and SENS2; Table 2), and the result of the SENS1 (or SENS2) experiment is subtracted from the CTL experiment (real conditions of 2017; Table 2). Thus, the impact of land–atmosphere coupling on circulation during extreme drought can be well isolated.

The time segment during which the wetness is imposed over ASLB is selected through the following considerations: 1) the soil dryness over ASLB began from March, which occurred earlier than the dryness over NEC, and 2) the interaction between soil moisture and atmospheric circulation over ASLB is more obvious during May–July than during March–April (Zeng et al. 2019). Accordingly, the artificial wetness is imposed during March–May. For every time step in the WRF experiment during March–May, precipitation values over ASLB are artificially multiplied by 5 before they reach the land surface, thereby soil moisture in the land surface model evolves

TABLE 2. Brief summary of the WRF simulations performed in this study.

Exp.	Simulation period	Analysis period	Soil moisture setting
CLIM	25 Feb–31 Jul for 1981–2010	1 Mar–31 Jul of each year	Coupled freely
CTL	25 Feb–31 Jul 2017	1 Mar–31 Jul 2017	Coupled freely
SENS1	25 Feb–31 Jul 2017	1 Mar–31 Jul 2017	1 Mar–31 May (precipitation over ASLB is artificially multiplied by 5 before reaching the land surface) 1 Jun–31 Jul (coupled freely)
SENS2	25 Feb–31 Jul 2017	1 Mar–31 Jul 2017	1 Mar–31 May (soil moisture values over ASLB are reset to climatological mean values every day) 1 Jun–31 Jul (coupled freely)

from dry to wet continuously for a period of 3 months. During June–July, the soil moisture is allowed to couple with the atmosphere freely (Table 2). Thus we can explore the nonlocal effect of antecedent land–atmosphere coupling over ASLB on the consequent drought over NEC. In SENS2, for the first time step of every day in the WRF experiment during March–May, the soil moisture values for four soil layers over ASLB are reset to the daily climatological mean values from the CLIM output data. Take 1 March as an example: for each model grid point, we average 30 daily mean soil moisture values on every 1 March from 1981 to 2010, and the averaged value is used to replace the soil moisture value at 0000:00 UTC 1 March 2017 in SENS2 (Table 2). In doing so, the nonlocal effect of upstream dry anomaly on the drought over NEC can be well extracted quantitatively. In addition, we found the surface sensible heating effect on atmosphere is strongest in May in the reanalysis data (Zeng et al. 2019), so the analysis in this study mainly focuses on the precipitation and circulation during May–July.

Before conducting the CLIM, CTL, SENS1, and SENS2 simulations, the cumulus convection schemes are tested because they have important impact on the precipitation simulation (Jankov et al. 2005; Liang et al. 2012; Yuan et al. 2012; Lu et al. 2019). To improve the 2017 NEC drought simulation, we first selected 2012, which has the second most precipitation over NEC since 1981, as a wet year, and then we tested nine cumulus convection schemes (Table 3) for capturing the precipitation difference between 2012 and 2017.

c. The LBM and experimental design

Fully nonlinear regional climate models, like the WRF Model, are getting more and more realistic, by which we can simulate and understand a number of feedback processes in current climate system. But if we want to interpret the cause-and-effect relationship between the forcing variable and the response variable thoroughly, it is difficult to carry out model output analysis directly. The linearized atmospheric model (e.g., LBM) aims to help understanding the complicated sequence of feedback in the dynamical atmosphere. A linear baroclinic model is usually used to examine the linear response of large-scale circulation to external diabatic heating anomalies (Watanabe and Jin 2003). The linearized primitive equation in LBM is symbolically written as

$$\mathbf{X}' = \mathbf{L}^{-1} \mathbf{F}', \quad (1)$$

where \mathbf{X}' is the vector that represents the anomaly response of atmospheric variables (e.g., disturbance vorticity, potential height, and temperature relative to the basic state, etc.), \mathbf{L} is the linear operator which depends on basic flow, and \mathbf{F}' is the anomaly of external heating.

In this study, the LBM is run with a T42 horizontal resolution and 20 vertical levels in the sigma coordinate. The LBM experimental design is shown as a schematic diagram in Fig. 2. The basic flow is derived from the May–July climatology of ERA-Interim reanalysis (including U , V , W , T , and surface pressure). The term \mathbf{F}' is the idealized diabatic heating anomalies during May–July of 2017 over ASLB; it mimics the vertical and horizontal distributions of heating in the atmosphere under wet and dry land surface conditions. Three different vertical heating patterns with elliptical horizontal distribution over ASLB are designed to force the LBM (Fig. 2). The first pattern refers to the profile with cooling effect in both lower and upper levels; it corresponds to the result in WRF SENS simulation (Fig. 2). The second pattern refers to the profile with lower heating and upper cooling and corresponds to the result in the WRF CTL simulation (Fig. 2). The third pattern refers to a profile with lower heating and upper zero, which is set to study the synergistic effect of upper cooling and lower heating by comparing with the second experiment (Fig. 2).

d. Calculations of diabatic heating and associated potential vorticity generation

To compare the dynamic and thermal differences between the CTL and SENS simulations, diagnosis processing is applied to the data outputted by the WRF Model. To explore the effect of surface sensible heat on the atmosphere, the diabatic heating rate Q_1 (K s^{-1}) can be obtained by an inverse calculation

TABLE 3. The list of convective parameterization schemes.

Convective parameterization schemes	
1	Betts–Miller–Janjic (Vaidya and Singh 2000)
2	Kain–Fritsch (KF) (Kain 2004)
3	Grell–Freitas (Grell and Freitas 2014)
4	Grell–3D (Grell and Dévényi 2002)
5	Tiedtke (Tiedtke 1989)
6	KF–CuP (Berg et al. 2013)
7	Multiscale KF (Zheng et al. 2016)
8	New SAS (Han and Pan 2011)
9	New Tiedtke (Zhang and Wang 2017)

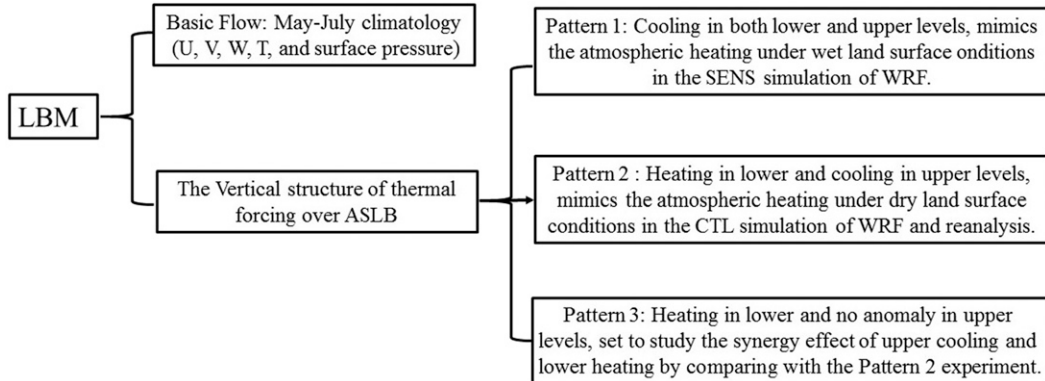


FIG. 2. A schematic diagram of the LBM experimental design to explore the steady response of circulation to wet and dry land surface conditions under specific basic flows.

method based on the thermodynamic equation in pressure coordinates (Yanai and Tomita 1998; Ren et al. 2015):

$$Q_1 = \frac{\partial T}{\partial t} + V_h \cdot \nabla_h T + \omega \left(\frac{\partial T}{\partial p} - \frac{RT}{c_p p} \right), \quad (2)$$

where the three items on the right side of (2) represent different contributed sources of Q_1 , of which the first is local change of air temperature (T ; in units of K), the second is the horizontal transfer of T due to meridional and zonal wind (V_h ; m s^{-1}), and the third is the vertical transport of T and buoyancy induced by vertical velocity ω (Pa s^{-1}), where R is the gas constant [$\approx 8.314 \text{ J} (\text{mol K}^{-1})^{-1}$], c_p is specific heat at constant pressure [$\approx 1.004 \text{ J} (\text{kg K}^{-1})^{-1}$], and p is the pressure (Pa). The unit of Q_1 is converted to kelvins per day (K day^{-1}) in this study.

Diabatic heating can influence the atmospheric motion by changing the thermal structure, which can be described by the potential vorticity (PV) equation as follows:

$$\begin{aligned} \frac{\partial \text{PV}}{\partial t} = & - \underbrace{\left(u \frac{\partial \text{PV}}{\partial x} + v \frac{\partial \text{PV}}{\partial y} \right)}_{\text{part-h}} - \underbrace{\omega \frac{\partial \text{PV}}{\partial p}}_{\text{part-w}} - g(f + \zeta) \frac{\partial Q_1}{\partial p} \\ & - g \left(\zeta_x \frac{\partial Q_1}{\partial x} + \zeta_y \frac{\partial Q_1}{\partial y} \right). \end{aligned} \quad (3)$$

PV (unit: PVU; $1 \text{ PVU} = 10^{-6} \text{ m}^2 \text{s}^{-1} \text{K kg}^{-1}$) can be written as

$$\text{PV} \cong -g(f + \zeta) \frac{\partial \theta}{\partial p}, \quad (4)$$

where $f (\text{s}^{-1})$ and $\zeta (\text{s}^{-1})$ are the Earth rotation vorticity and the relative vorticity respectively, and $\theta (\text{K})$ is isobaric potential temperature. PV is conserved in frictionless and adiabatic motion. The positive (negative) anomaly of PV corresponds to cyclonic (anticyclonic) circulation anomaly. According to our previous PV budget diagnosis (Zeng et al. 2019), the negative PV anomaly (anticyclonic) resulting in NEC drought is mainly attributed to the third term on the right side of (3). This term is directly related to the increase or decrease of PV due to external heat source, which is called PV generation (PVG).

Thereby, we only focus on PVG in this study, and the horizontal (part-h) and vertical (part-w) transportation of PV will be neglected. Similar to Ren et al. (2015), PVG can be linearized as follows:

$$\text{PV}'_{\text{PVG}} = -g(f + \bar{\zeta}) \frac{\partial Q'_1}{\partial p} - g\zeta' \frac{\partial \bar{Q}_1}{\partial p} + \text{residues}_Q, \quad (5)$$

where a variable is decomposed into its climatological mean (denoted with overbar) and its annual anomaly (denoted with a prime). Previous studies have shown that on the right side of (5), the first term is the main contributor to PV'_{PVG} (Ren et al. 2015), which is determined by the climatological mean of absolute vorticity and by the interannual anomaly of vertical diabatic heating rate gradient. Therefore, $-g(f + \bar{\zeta})(\partial Q'_1/\partial p)$ is calculated and regarded as PV'_{PVG} hereafter.

3. Results

a. The NEC drought in the WRF control simulation

The observational precipitation difference between the chosen dry year (2017) and wet year (2012) of NEC is shown in Fig. 3a, and the differences in simulations with nine convective parameterization schemes are shown in Figs. 3b–j. There are obvious negative precipitation differences over both NEC and ASLB in observation (Fig. 3a), which is consistent with the drought event occurring concurrently over the two regions in 2017. Most schemes can simulate the concurrent negative precipitation anomalies over NEC and ASLB except for the Tiedtke and new simplified Arakawa–Schubert (New SAS) schemes, with positive (negative) anomalies over NEC (ASLB) in Tiedtke (Fig. 3f) and negative (positive) anomalies over NEC (ASLB) in New SAS (Fig. 3i). To find the optimal scheme for simulating a negative precipitation anomaly over NEC, the regional averaged values over NEC in Figs. 3a–j are shown by bar graphs in Fig. 3k. It is found that Kain–Fritsch exhibits the strongest negative value and has the smallest absolute error (0.2 mm day^{-1}). For the regional averaged values of ASLB (Fig. 3l), the Kain–Fritsch scheme also shows the strongest negative value and smallest absolute error (0.12 mm day^{-1}).

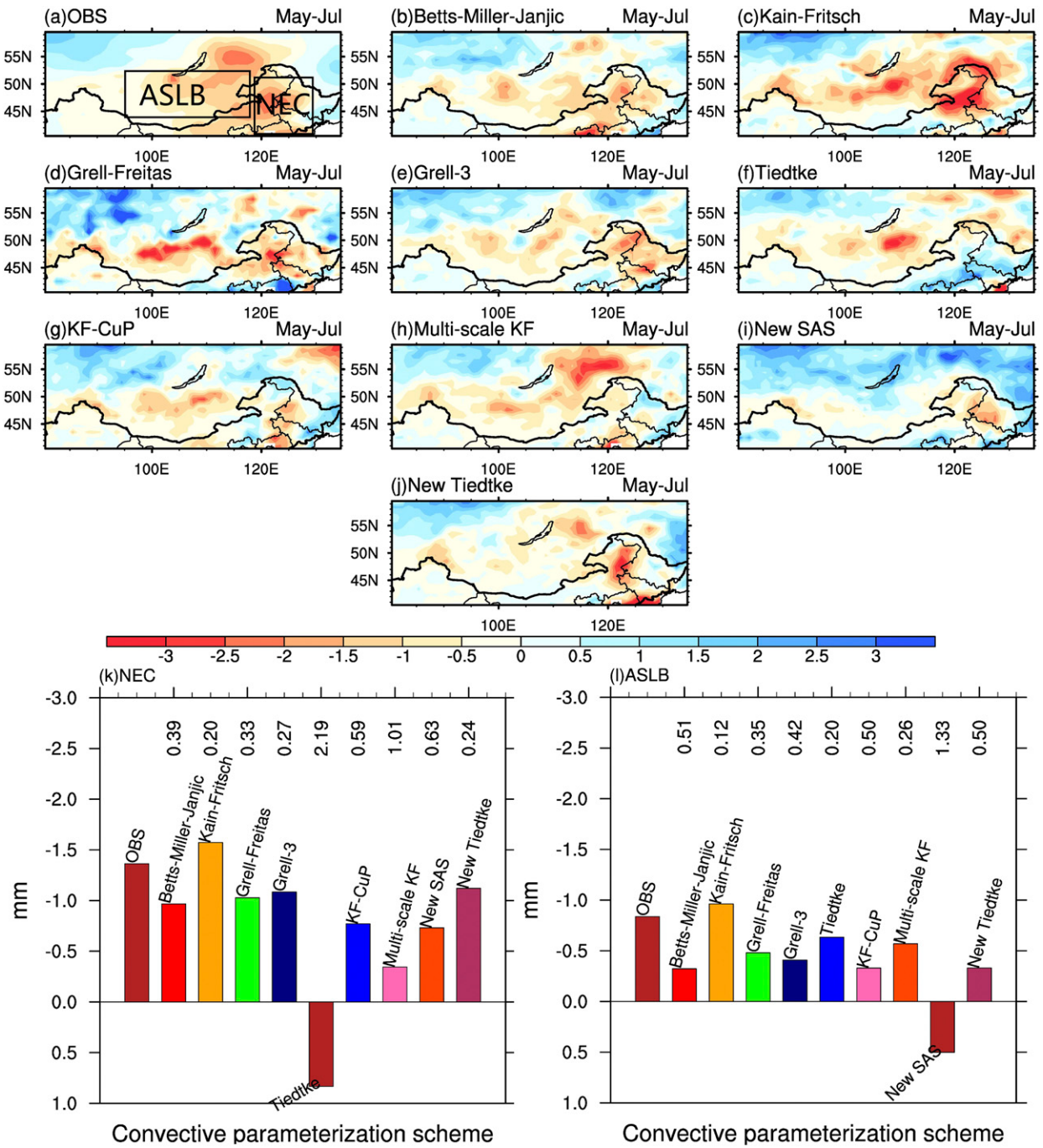


FIG. 3. The differences in May–July mean precipitation (mm day^{-1}) between 2017 (dry year) and 2012 (wet year) from (a) observation and (b)–(j) WRF simulations with nine different convection schemes listed in Table 3. Also shown is the May–July mean precipitation averaged over (k) Northeast China (NEC) and (l) the area south of Lake Baikal (ASLB) marked as boxes in (a). The values above each bar in (k) and (l) are the absolute errors compared with observation.

So we selected Kain–Fritsch as the final convective parameterization scheme for the WRF CLIM, CTL, and SENS experiments.

The 2-m air temperature (T2m) differences between the dry year (2017) and wet year (2012) of NEC in observation and the

optimization test are also shown in Fig. 4. It is found that NEC shows weak positive or negative T2m differences while ASLB shows strong positive differences (Fig. 4a). The model output data present a similar distribution: most schemes show strong positive differences over ASLB and moderate differences over

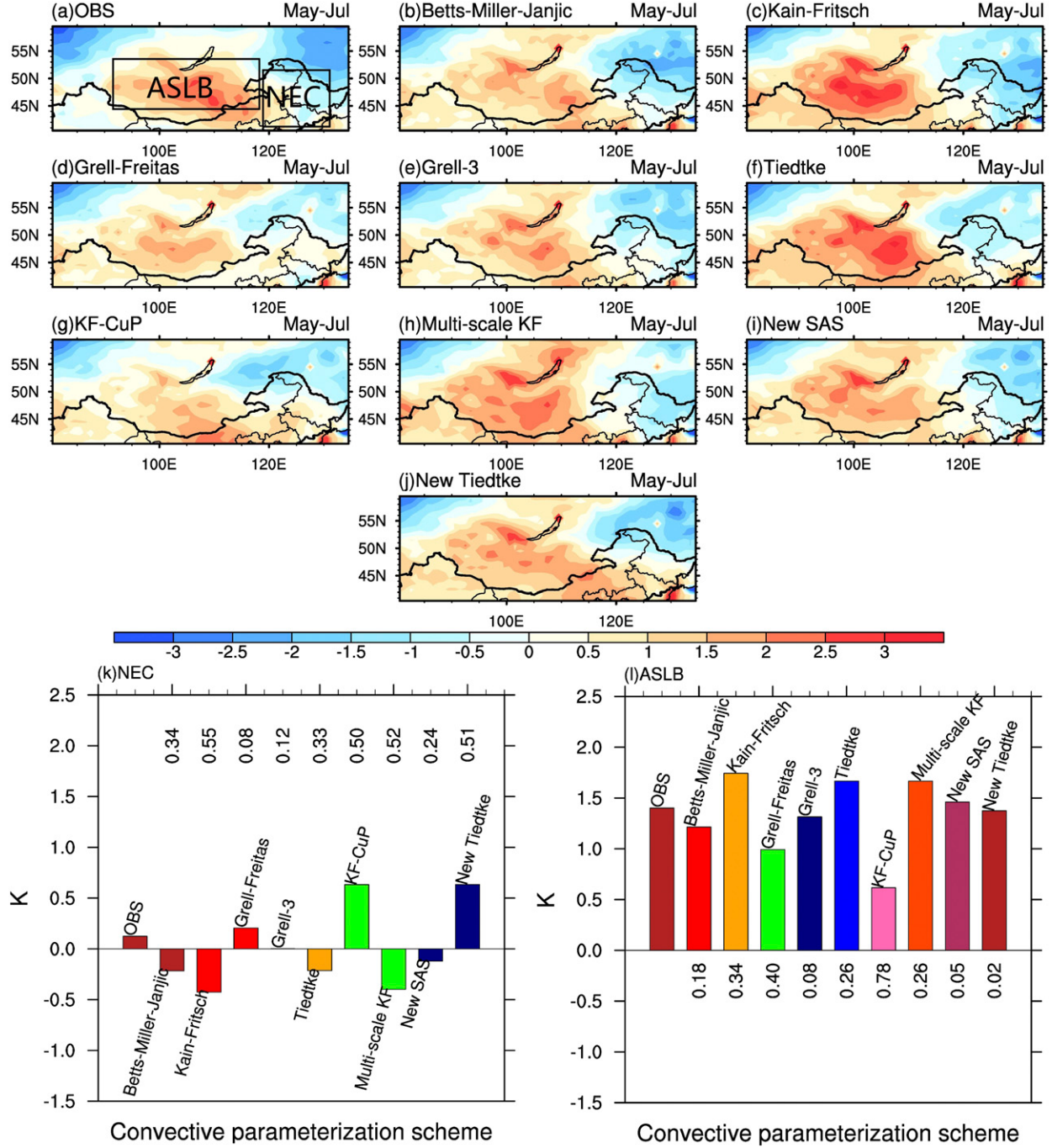


FIG. 4. As in Fig. 3, but for May–July mean 2-m air temperature (T2m; K).

NEC (Figs. 4b–j). The significant positive T2m anomaly is a result of the surface sensible heat anomaly induced by land–atmosphere feedback during drought (Zhou et al. 2019). Here the strong (weak) difference over ASLB (NEC) indicates that more (less) significant land–atmosphere coupling exists over ASLB (NEC) in the 2017 NEC drought. The regional average values (Figs. 4k,l) are consistent with the spatial distributions. It is worth noting that Kain–Fritsch shows the largest positive

T2m difference over ASLB (Fig. 4l), which agrees well with the largest negative precipitation difference in Fig. 3l.

Figures 5a and 5b show the observed precipitation and circulation anomaly in May–July during 2017. The negative precipitation anomaly shows a zonal distribution over ASLB and NEC, with a maximum center over the two regions (Fig. 5a). The 500-hPa geopotential height shows positive anomalies over NEC and ASLB and an anticyclonic anomaly center over

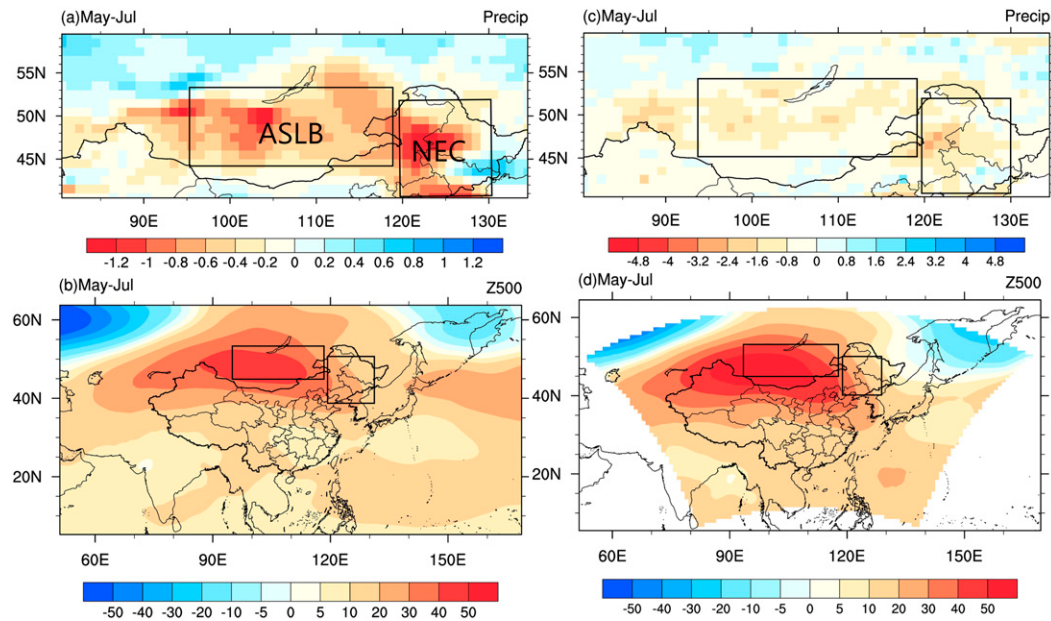


FIG. 5. (a) Observed precipitation anomalies (CMAP; mm day^{-1}) and (b) reanalyzed geopotential height anomalies (ERA-Interim; gpm) at 500 hPa in May–July during 2017. The climatology used for calculating the anomalies is 1981–2010. (c),(d) As in (a) and (b), but for the WRF simulated differences between 2017 (from CTL experiment) and the climatology (1981–2010, from the CLIM experiment).

ASLB (Fig. 5b). In the anomaly field of CTL in comparison with CLIM, the above patterns can be well simulated (Figs. 5c,d).

Reanalyzed 0–100-cm soil moisture anomalies during March–July of 2017 are shown in Figs. 6a–e. Soil drought occurs over ASLB from March to July of 2017, and becomes more severe over time, which is highly consistent with the simulation of soil moisture anomaly from CTL experiment (Figs. 6f–j). Over NEC, however, WRF simulates weak wet anomalies during March–May and dry anomalies during June–July. This is a little different from reanalysis, in which the dry anomaly appears from April. So both the reanalysis and WRF simulation suggest that the soil dryness over ASLB occurs earlier than that over NEC, which provides a reasonable base for the sensitivity experiments regarding the effect of land–atmosphere coupling over ASLB on downstream drought.

b. WRF simulation of the responses to imposed land surface wetness

From the above analysis, it is found that negative soil moisture anomaly over ASLB is initialized in March of 2017, indicating that the soil dryness starts to accumulate then. So the SENS experiment aims to weaken this dryness to explore the impact on the downstream areas. SENS is conducted based on the following assumptions: when an artificial wetness is continually imposed over ASLB in WRF model during March–May, the mitigated soil dryness will continue to June–July due to the memory of soil moisture; thus the local surface sensible heating on the low-level atmosphere will be reduced, and the anticyclonic circulation anomaly (Fig. 5d) over ASLB will be weakened during May–July, ultimately relieving the NEC drought.

Figure 7 depicts the precipitation and 500-hPa geopotential height differences by subtracting WRF SENS1 (SENS2) simulation results from the WRF CTL simulation results (i.e., dry case minus wet case). We found that significant negative precipitation anomalies distribute in a narrow and zonal belt from ASLB to NEC both in SENS1 and SENS2 (Figs. 7a,c). The corresponding 500-hPa circulation shows positive geopotential height anomalies (anomalous anticyclone) over the two regions (Figs. 7b,d), especially over ASLB in SENS2 (Fig. 7d), where the spatial distribution is similar to the anomalies of CTL (Fig. 5d).

The above results indicate that the antecedent (March–May) upstream (ASLB) soil dryness (soil in the CTL simulation is drier than that in the SENS simulation) is critical for maintaining the intensity of consequent (May–July) drought over the downstream region (NEC), and the atmospheric circulation anomaly may act as a medium. From the longitude–time evolution of circulation anomaly over the latitudinal zone of 40° – 60° N (Fig. 8), eastward propagation of positive geopotential height anomalies from 90° to 135° E can be found during June–July, indicating that the atmospheric response began in the middle of June, which obviously exists in both the SENS1 and SENS2 (marked with black lines in Figs. 8a and 8b) simulations. This is also consistent with the conclusion based on reanalysis data (Zeng et al. 2019), where the strongest coupling between atmospheric circulation and soil moisture occurred during June and July over ASLB.

Because SENS2 can approximately isolate the contribution of upstream soil moisture anomaly to downstream atmospheric circulation anomaly, we calculated the regional averaged values of Z500 over ASLB and NEC, respectively (Table 4).

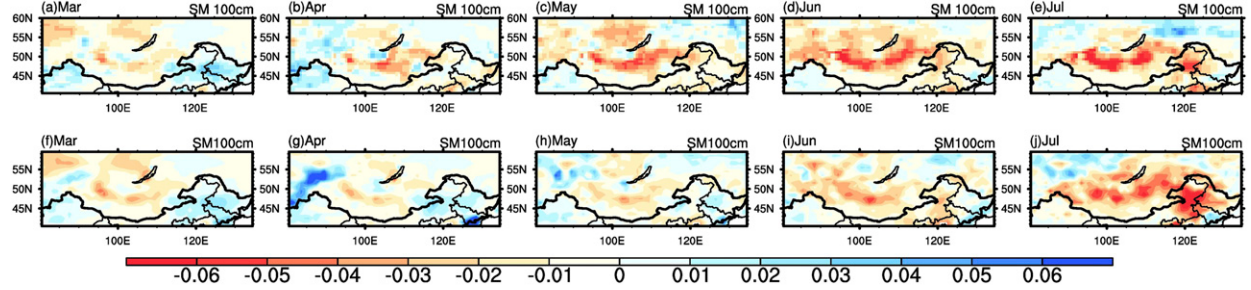


FIG. 6. Reanalyzed 0–100-cm soil moisture anomalies (ERA-Interim; $\text{m}^3 \text{m}^{-3}$) during (a)–(e) March–July 2017, respectively. (f)–(j) As in (a)–(e), but for the WRF-simulated differences between 2017 (from CTL experiment) and the climatology (1981–2010, from the CLIM experiment).

The values of $\text{CTL} - \text{CLIM}$ can be considered as the signal forced by all the external factors, while the values of $\text{SENS2} - \text{CLIM}$ contains all factors except soil moisture anomalies, so $(\text{CTL} - \text{CLIM}) - (\text{SENS2} - \text{CLIM})$ can represent the absolute contribution made by soil moisture. The differences in geopotential height between CTL and SENS2 are 17.51 gpm over ASLB and 13.79 gpm over NEC, and the relative contributions are 40.99% over ASLB and 71.56% over NEC (Table 4). We also find the spatial distribution of Z500 in SENS2 – CLIM (Fig. S1a) in the online supplemental material has a similar but weaker pattern to that in CTL – CLIM (Fig. 5d). The spatial distribution of precipitation in SENS2 – CLIM (Fig. S1b) is also similar to that in CTL – CLIM (Fig. 5c), and the relative contributions of soil moisture to precipitation deficit are 72.46% over ASLB and 65.44% over NEC (Table 5). To further investigate the underlying

processes, the land surface differences between the CTL and SENS1 (SENS2) experiments are shown in Fig. 9. A remarkable negative soil moisture anomaly exists around Lake Baikal (mainly over ASLB) during May–July, and a less prominent negative anomaly exists over NEC (Figs. 9a,c). Drier soil moisture usually corresponds to more surface sensible heat flux, which is the case over ASLB with strong positive anomaly (Figs. 9b,d). Over NEC, however, there is no pronounced positive anomaly of sensible heat, with most regions dominated by weak negative anomaly (Figs. 9b,d). Thus, the two sensitivity experiments both show a strong surface dryness over ASLB instead of NEC (Fig. 9). This is similar to the results of sensitivity experiments of convection schemes (Figs. 3 and 4), where most schemes show strong negative precipitation anomaly over both ASLB and NEC regions, while showing strong positive T2m anomaly only over ASLB. This indicates

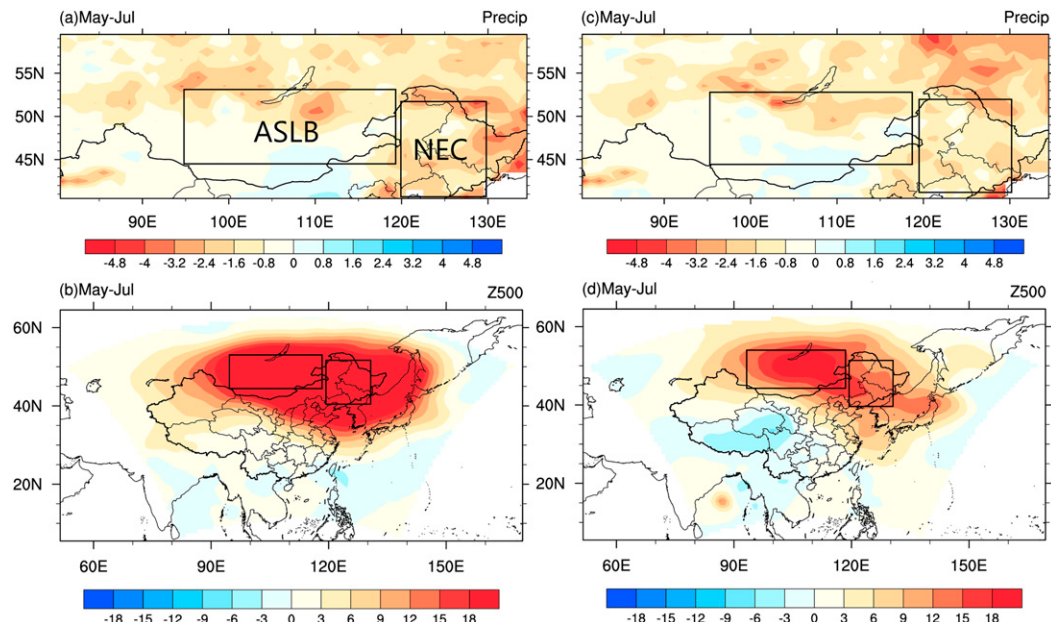


FIG. 7. WRF simulated differences in May–July mean anomalies of (a) precipitation (mm day^{-1}) and (b) geopotential height (gpm) at 500 hPa between the CTL and SENS1 simulations ($\text{CTL} - \text{SENS1}$) during 2017. (c),(d) As in (a) and (b), but for the differences between CTL and SENS2 simulations ($\text{CTL} - \text{SENS2}$).

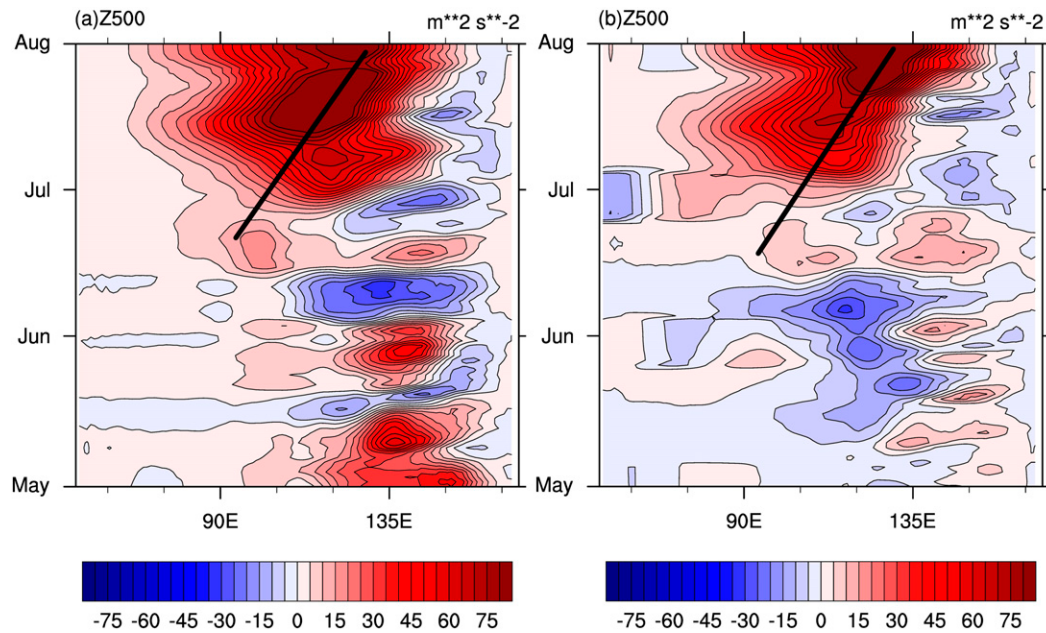


FIG. 8. Longitude–time diagram for 15-day running mean of the May–July geopotential height differences averaged over 40° – 60° N. (a) Differences between the CTL and SENS1 simulations (CTL – SENS1), and (b) differences between CTL and SENS2 simulations (CTL – SENS2). The black lines in (a) and (b) indicate that the height anomalies propagate from upstream regions (ASLB) to downstream regions (NEC) during June–July.

that the land–atmosphere coupling induced surface sensible heating is more significant over ASLB than over NEC during the 2017 extreme drought event.

From the monthly evolution of soil moisture at various depths (0–10, 10–40, and 40–100 cm; Figs. S2 and S3), both the CTL – SENS1 and CTL – SENS2 results show that a remarkable negative soil moisture anomaly exists over ASLB throughout the drought period (April–July), whereas the negative anomaly starts to present over NEC at the end of the drought (July).

To examine how the surface heating anomaly changes the thermal and dynamic structure of the lower atmosphere, we analyze the Q_1 (diabatic heating rate) anomaly at 850 hPa and the PVG (PV generation) anomaly at 750 hPa in atmosphere (Fig. 10). Unlike the differences of CTL minus SENS1 shown in Figs. 7 and 8, here the anomaly is calculated by subtracting the CTL and SENS1 results from the CLIM results respectively, and thus we can explore whether the atmospheric responses to dry and wet surface anomalies are symmetric.

In the CTL experiment, anomalous sensible heat is transported into the planetary boundary layer because of the soil dryness over ASLB during May to July, thus a heating source is formed in the lower troposphere at 850 hPa (Fig. 10a). This is more evident in the regional averaged vertical heating profile over ASLB with a maximum at 850 hPa (Fig. 11a). A strong cooling anomaly can also be found at 650 hPa in this profile (Fig. 11a). This is because the upper-level anticyclonic anomaly is usually combined with anomalous sinking motion, which leads to a reduction of cloud amount, thus less surface long-wave radiation will be absorbed by the atmosphere (not shown), and Q_1 appears as a negative anomaly relative to climatology in the upper level (Fig. 11a). This “upper cooling and lower heating” pattern means that $(\partial Q'_1/\partial p) > 0$. According to Eq. (5), it will lead to negative PVG over ASLB (Fig. 10c). PVG can be used to diagnose the contribution of diabatic heating to local PV anomaly qualitatively, where positive (negative) PVG is beneficial to the maintenance of cyclonic (anticyclonic) anomaly. So in the CTL simulation, negative

TABLE 4. The contribution of ASLB soil moisture anomalies to potential height anomalies at 500 hPa over local (ASLB) and downstream (NEC) regions.

Expt	ASLB	NEC
CTL – CLIM	42.72 gpm	19.27 gpm
SENS2 – CLIM	25.21 gpm	5.48 gpm
Absolute contribution (CTL – SENS2)	17.51 gpm	13.79 gpm
Relative contribution [(CTL – SENS2)/(CTL – CLIM)]	40.99%	71.56%

TABLE 5. The contribution of ASLB soil moisture anomalies to precipitation deficit over local (ASLB) and downstream (NEC) regions.

Exp.	ASLB	NEC
CTL – CLIM	$-1.38 \text{ mm day}^{-1}$	$-2.17 \text{ mm day}^{-1}$
SENS2 – CLIM	$-0.38 \text{ mm day}^{-1}$	$-0.75 \text{ mm day}^{-1}$
Absolute contribution (SENS2 – CTL)	-1.0 mm day^{-1}	$-1.42 \text{ mm day}^{-1}$
Relative contribution [(SENS2 – CTL)/(CTL – CLIM)]	72.46%	65.44%

PVG over ASLB indicates that sensible heating makes a positive contribution to the local low-level anticyclonic circulation anomaly.

In the SENS1 simulation, when the soil is artificially wetted at an earlier stage (March–May), the soil moisture may act as a cooling source in low-level atmosphere over ASLB during the later stage (Fig. 10b). The vertical profile of Q_1 is changed and shows a cooling effect in both upper and lower levels (Fig. 11b), and the vertical gradient ($\partial Q'_1 / \partial p < 0$) will lead to a positive PVG (Fig. 10d), which is against the maintenance of anticyclonic anomaly over ASLB. Compared with the result of the CTL simulation (Figs. 10a,c and 11a), it is found that when the surface heating is reduced over ASLB, the positive geopotential height anomaly will decrease due to the changed vertical heating profile.

c. LBM simulation of the responses to idealized diabatic heating anomaly

To isolate the influence of land–atmosphere coupling on NEC drought from the other factors (e.g., midlatitude teleconnection

from upstream area, polar sea ice, and tropical SST anomalies, etc.), we have analyzed the result of CTL simulation minus the SENS1 (SENS2) simulation (Figs. 7–9). But these results essentially contain a series of feedback processes related to land–atmosphere interaction, such as the feedback between soil moisture and surface flux, between surface flux and boundary layer, and between boundary layer and cloud in the upper atmospheric level. Thereby, to illustrate the cause-and-effect relationship between the surface anomaly and atmospheric circulation more clearly, here we drive the LBM with an ideal heat source without regard for complex coupling.

According to the above PVG analysis in section 3b, we know the anomalies of diabatic heating in the low-level atmosphere related to surface thermal conditions are symmetric, manifesting as a heating (cooling) anomaly under a dry (wet) soil anomaly (Fig. 11). So in this section, three LBM experiments are performed as mentioned in section 2c, in which the May–July mean atmosphere is forced with idealized diabatic heating anomalies over ASLB, and the anomalies can mimic the atmospheric heating associated with different land surface

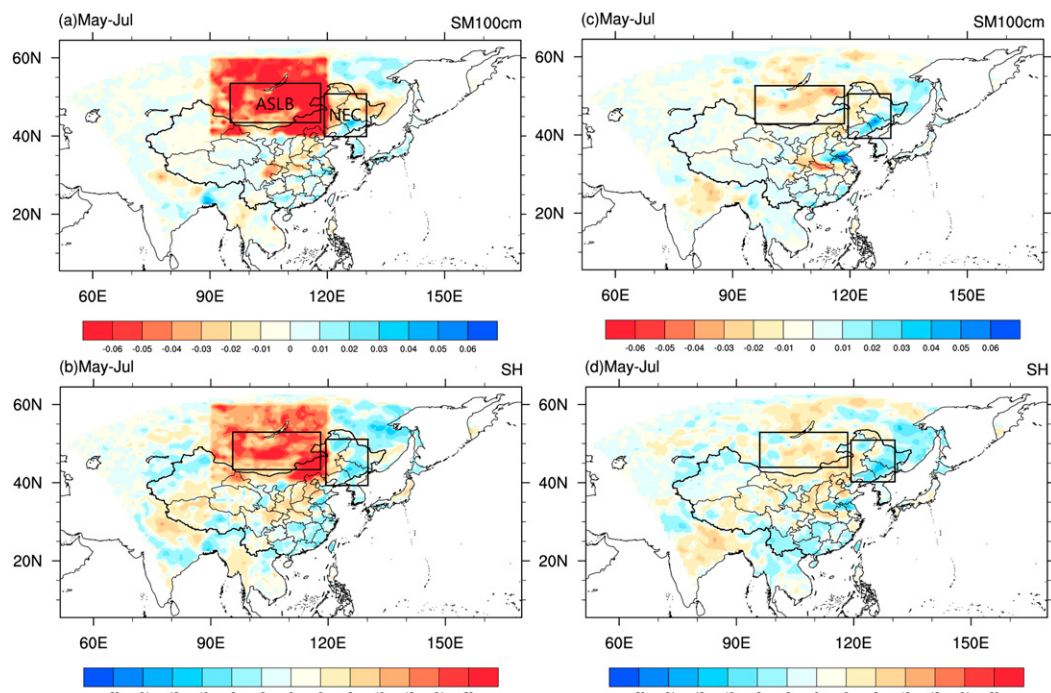


FIG. 9. WRF simulated differences in May–July mean (a) 0–100-cm soil moisture ($\text{m}^3 \text{ m}^{-3}$) and (b) surface sensible heat flux (W m^{-2}) between the CTL and SENS1 simulations (CTL – SENS1) during 2017. (c), (d) As in (a) and (b), but for the differences between CTL and SENS2 simulations (CTL – SENS2).

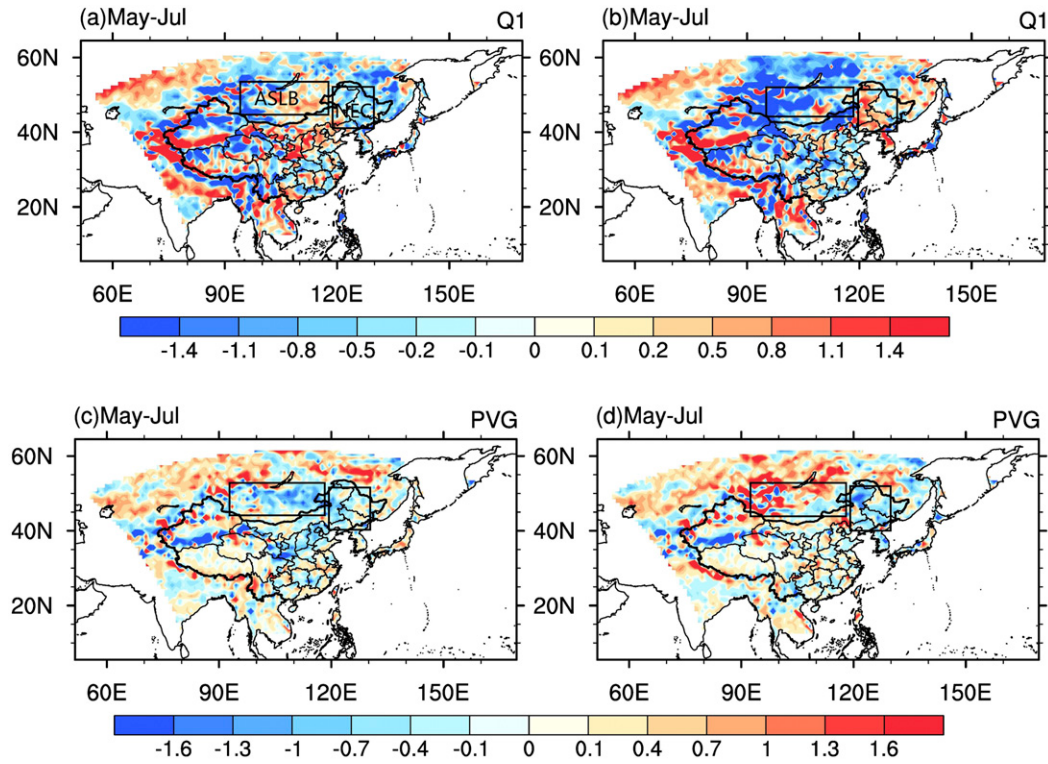


FIG. 10. WRF simulated differences in (a) atmospheric diabatic heating rate Q_1 (K day^{-1}) at 850 hPa and (c) PV generation [$\text{PV}'_{\text{PVG}} = -g(f + \bar{\zeta})(\partial Q'_1 / \partial p)$; $10^{-1} \text{ PVU day}^{-1}$] at 750 hPa between CTL and CLIM simulations. (b),(d) As in (a) and (c), but for the differences between SENS1 and CLIM simulations.

anomaly relative to climatology. Because the heating or cooling anomalies induced by soil moisture anomalies are closed to the ground, here we set the maximum idealized diabatic heating (cooling) at the level $\sigma = 0.99$ in the vertical coordinate

(Figs. 12a–c), and this setting is reasonable and in line with previous research (Koster et al. 2016). The profile in Fig. 12a is consistent with that of SENS1 simulation (Fig. 11b), manifested as cooling effect in both upper and lower levels. The

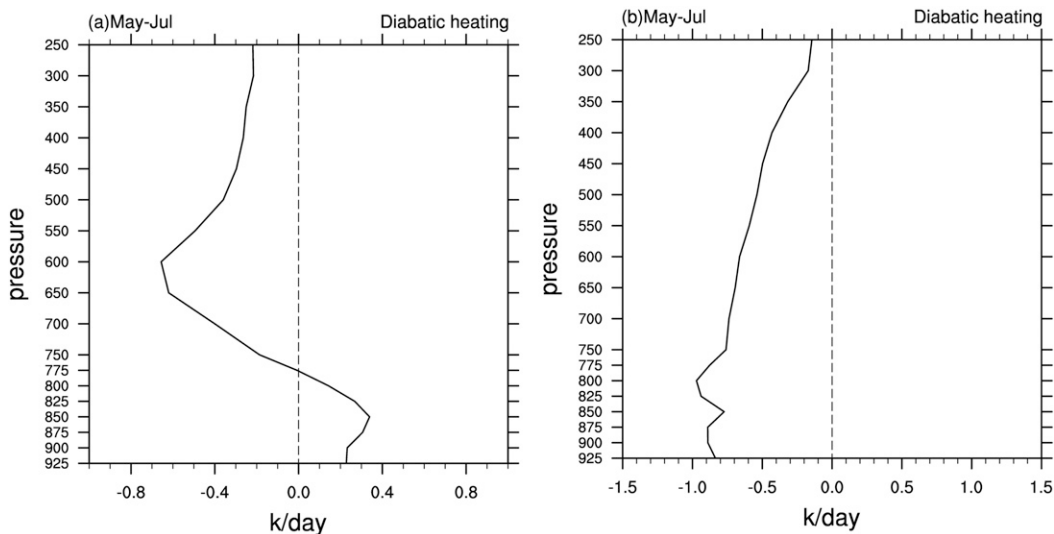


FIG. 11. Vertical profiles of diabatic heating Q_1 (K day^{-1}) averaged over the ASLB region marked by black boxes in Fig. 1: (a) the difference between the CTL and CLIM simulations and (b) the difference between SENS1 and CLIM simulations.

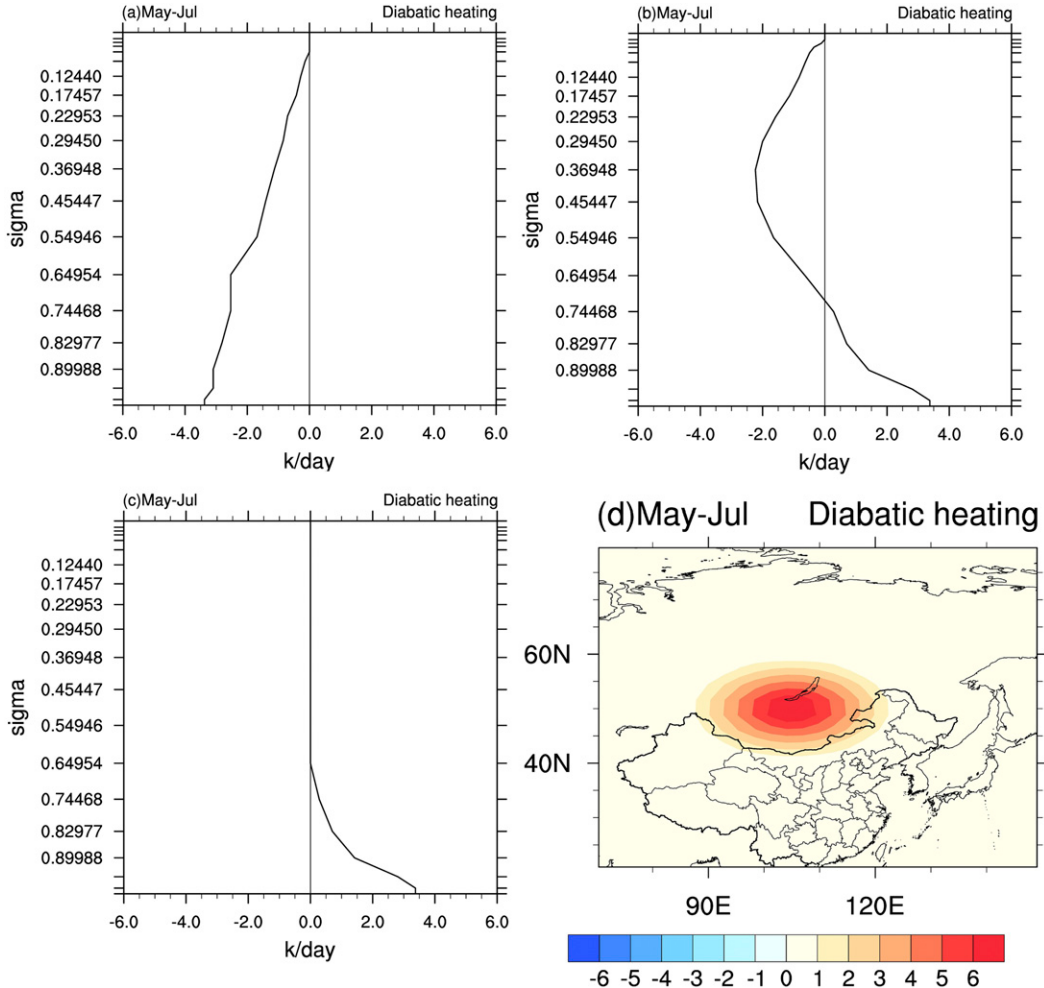


FIG. 12. Vertical profiles of idealized diabatic heating anomaly imposed in the LBM simulations over the ASLB region. (a) Cooling effect in both upper and lower levels, which corresponds to differences between the SENS1 and CLIM simulations shown in Fig. 11b. (b) Heating effect in the lower level and cooling effect in the upper level, which corresponds to the differences between the CTL and CLIM simulations shown in Fig. 11a. (c) To further investigate the influences of upper cooling effect on the atmospheric circulation, we set a vertical profile that presents a heating effect in the lower level without an anomaly in the upper level. (d) The spatial distribution of imposed idealized heating anomaly (K day^{-1}).

linear steady response of 500-hPa geopotential height to this pattern is shown in Fig. 13a, with a negative anomaly over ASLB and NEC and the maximum center over NEC. The profile shown in Fig. 11b is consistent with the atmosphere heating of CTL simulation (Fig. 11a) as well as the reanalysis (now shown), which manifested as a cooling (heating) effect in the upper (lower) level. The steady response to this heating pattern shows a positive anomaly over ASLB and NEC with a maximum center over ASLB (Fig. 13b). Comparing this with the response pattern depicted in Fig. 13a, it shows the same spatial distribution but with a contrary sign. These two responses indicate the atmosphere heating associated with the soil dryness over ASLB can really excite positive potential height anomalies over the downstream region (NEC). To further investigate the role of upper-level cooling mimicked in

Figs. 11a and 12b, we force the LBM by an idealized heating with heating in lower level but no anomaly in upper level (Fig. 12c), and find that the response (Fig. 13c) is quite similar to the one forced by the “upper cooling and lower heating” pattern (Fig. 13b). When subtracting the latter (Fig. 13c) from the former (Fig. 13b), we can find a similar but weaker pattern (Fig. 13d) as Fig. 13c shows, indicating that the synergy of upper-level cooling and lower-level heating has a weak positive contribution to the high anomaly over NEC.

It should be noted that the LBM response patterns in Figs. 13b and 13c both show an anticyclonic anomaly center over the eastern region of ASLB (to the west of 120°E), which is basically consistent with the result of WRF CTL simulation minus SENS1 (SENS2) simulations (Figs. 7,d). This phenomenon responds well to the hypothesis below: the circulation anomaly in

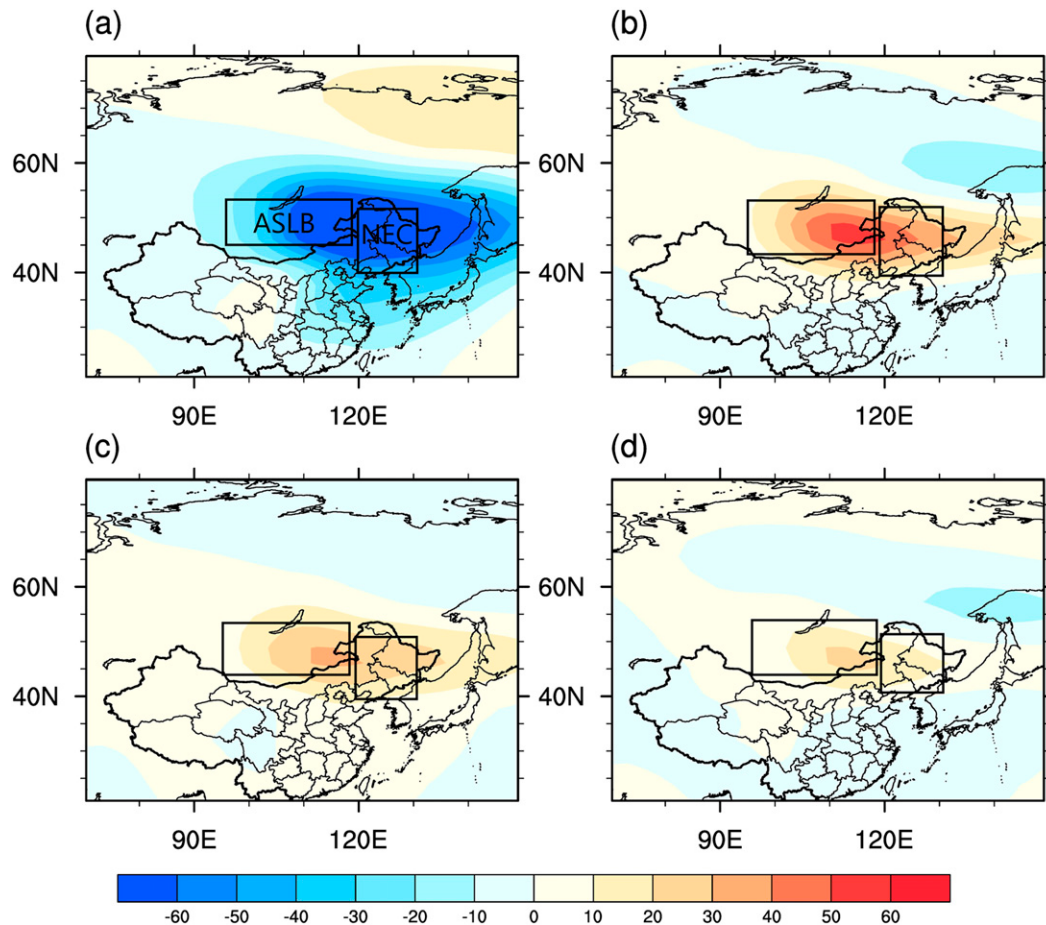


FIG. 13. The responses of geopotential height (gpm) at 500 hPa to the thermal forcing as Fig. 12 shows; the responses are produced by the LBM experiments for (a) Fig. 12a, (b) Fig. 12b, and (c) Fig. 12c. (d) The differences between (b) and (c).

the CTL simulation contains all impact factors of atmospheric circulation (Fig. 5d) resulting in NEC drought (Fig. 5c), while the values of CTL simulation minus SENS1 (SENS2) simulations only reserve the circulation response due to anomalous land-atmosphere coupling (Figs. 7b,d). The LBM simulated responses also only contain the signal from anomalous thermal forcing related to soil dryness. We notice that the anomaly center over ASLB locates more westward in Fig. 7d (CTL – SENS2) than in Fig. 7b (CTL – SENS1) and in Figs. 13b and 13c (LBM), which is most similar to the circulation anomaly in CTL simulation (Fig. 5d). So Fig. 7d shows the most reasonable response, because the setting of artificial soil wetness in SENS2 is much closer to the climatology reality. The eastward shifts of Z500 positive anomalies in SENS1 and LBM are probably because of the vertical distribution of ideal heating source in LBM, the coarse horizontal resolution of LBM (T42), and the shape or strength of artificial wetness in SENS1.

We also selected all the spring–summer persistent drought events over NEC during 1981–2017, defined as having standardized precipitation anomalies in spring (March–May) and summer (June–July) both lower than -0.4 . These droughts

occurred in 1987, 1992, 1999, 2000, 2001, 2004, and 2017 and are marked by a black box in Fig. 14a. We found that 2017 is indeed the most extreme year, with the standardized precipitation anomaly lower than -1.0 both in spring and in summer. To further investigate the persistence of forcing from upstream soil moisture anomalies, Fig. 14b shows the monthly evolution of standardized soil moisture anomaly averaged over ASLB in each event. Again, 2017 is a unique year in which the anomalies are negative in every month from March to July. But in other persistent drought years, most values are positive, and the strongest negative anomaly is smaller than -0.1 during March–May, and is small than -0.2 during June–July. These weak negative anomalies are much smaller than those in 2017. Above all, the duration and density of soil dryness over ASLB are unique during March–July of 2017. So our numerical simulations only focus on the 2017 NEC drought event.

4. Summary and discussion

In this study, the influence of upstream land–atmosphere coupling on the 2017 NEC persistent drought is investigated by

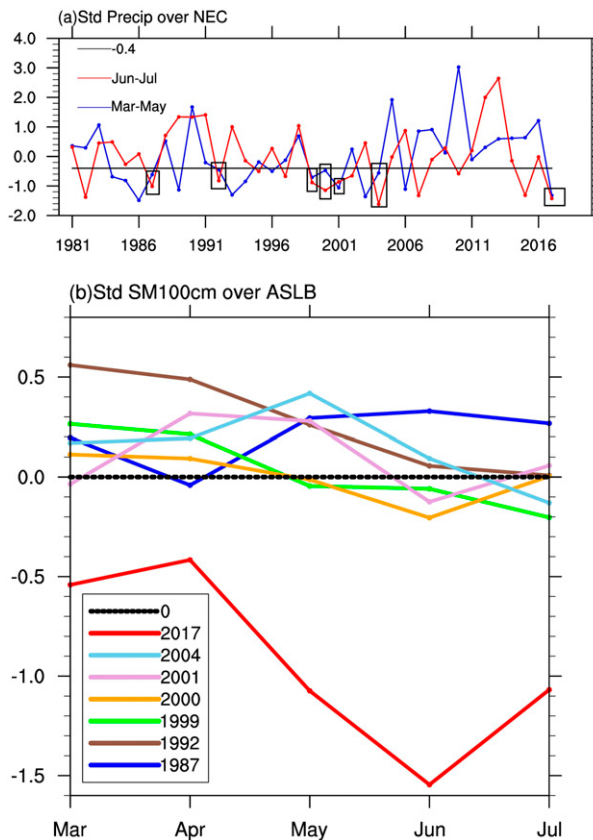


FIG. 14. (a) The time series of standardized March–May mean (blue) and June–July mean (red) precipitation anomalies averaged over Northeast China (NEC) region marked in Fig. 3a. The black line refers to the reference drought value (-0.4). Seven spring–summer drought events over NEC are marked by black boxes, with standardized precipitation anomalies in spring (March–May) and summer (June–July) both lower than -0.4 . (b) The monthly evolution of regional mean standardized anomalies of soil moisture (0–100 cm) over ASLB in the seven drought events.

means of regional climate model and LBM simulations, and the results provide a credible and coherent picture of key processes and mechanisms contributed to the drought: the land–atmosphere coupling over the upstream region (ASLB) in an earlier stage has played an important role in the intensity and persistence of drought occurred over the downstream region (NEC) through changing atmospheric circulation.

The NEC drought began in March and ended in July of 2017, and the land surface and atmosphere coupled with each other more significantly during May–July than March–April (Zeng et al. 2019). So here we mainly focus on the precipitation during May–July. In the WRF CTL simulation, the coherent precipitation and the circulation anomalies over ASLB and NEC can be well reproduced. The WRF simulated negative 0–100-cm soil moisture anomaly over ASLB begins in March, which appears earlier than that over NEC (May). This is basically identical with the evolution of soil moisture in reanalysis data, indicating that the cumulative effect of soil dryness over

the upstream region (ASLB) may be initialized at the beginning (March) of 2017 NEC drought. So in the SENS simulation, the soil moisture content over ASLB region is forced to be wet during March–May. Due to the memory of soil moisture, the local surface sensible heating in the low-level atmosphere decreases over ASLB during May–July, and thus the positive anomalies of geopotential height field over ASLB and NEC decrease, manifesting as an anticyclonic circulation anomaly over ASLB and NEC in the difference between the CTL and SENS1 (SENS2) simulations (Figs. 7b,d). Thus the NEC drought strength will decrease without dry land–atmosphere coupling over the upstream ASLB region (Figs. 7a,c). Tables 4 and 5 show that the soil dryness over ASLB contributed 65.44% to the precipitation deficit and 71.56% to the positive anomaly of geopotential height over the downstream region (NEC).

To separate the land forcing on the atmosphere from complex land–atmosphere coupling, the LBM is forced with ideal heat source, which mimics the atmospheric heating associated with dry soil anomaly in WRF CTL simulation. The quasi-steady response of circulation from LBM simulation (Fig. 13b) is highly consistent with the differences between the WRF CTL and WRF SENS simulations (Figs. 7b,d). The LBM simulation also shows that, besides the surface sensible heating, the upper cooling induced by reduced cloud only makes a small contribution to the high anomaly over NEC (Fig. 13d). In brief, our simulations reveal the mechanism through which the upstream land–atmosphere coupling influences the downstream drought, in which the atmospheric circulation acts as a medium.

Besides the “imposed-wetting” simulations in this study, a GLACE-1-type coupling experiment may also be helpful, in which we can compare the results between the simulations with free and inhibited land–atmosphere interaction (Koster et al. 2004). Furthermore, the NEC drought can also be affected by the reduced polar sea ice and snow cover in western Eurasia (S. Wang et al. 2019; Li et al. 2018), so their contributions could be investigated by changing the albedo of underlying surface in numerical model simulations.

How the surface anomalies modulate the atmospheric circulation and contribute to the spread of drought to other areas remain as key questions to uncover the importance of land–atmosphere feedback (Miralles et al. 2019). Our study shows a possible drought self-intensification and self-propagation mechanism, which implies that the influence the local surface anomaly exerts on the free atmosphere at a larger scale is important for sustaining an extreme drought. A reasonable simulation of upstream land–atmosphere coupling is critical for the downstream drought monitoring and forecast, especially for the land–atmosphere coupling hotspots over midlatitude regions, and for droughts at shorter time scales (e.g., flash droughts; Yuan et al. 2019). The multiscale nature of land–atmosphere coupling (Zeng and Yuan 2018) and droughts (Yuan et al. 2020) emphasizes the need for further investigation of their interactions.

Acknowledgments. This work was supported by the National Natural Science Foundation of China (41875105), the National Key R&D Program of China (2018YFA0606002), the Northwest Regional Numerical Forecasting Innovation Team Fund

(GSQXCXTD-2020-02), and the Startup Foundation for Introducing Talent of NUIST. We thank Dr. M. Watanabe and Dr. M. Hayashi for providing the LBM code.

REFERENCES

- Berg, A., B. Lintner, K. Findell, and A. Giannini, 2017: Soil moisture influence on seasonality and large-scale circulation in simulations of the West African monsoon. *J. Climate*, **30**, 2295–2317, <https://doi.org/10.1175/JCLI-D-15-0877.1>.
- Berg, L. K., W. I. Gustafson Jr., E. I. Kassianov, and L. Deng, 2013: Evaluation of a modified scheme for shallow convection: Implementation of CuP and case studies. *Mon. Wea. Rev.*, **141**, 134–147, <https://doi.org/10.1175/MWR-D-12-00136.1>.
- Chen, F., and Coauthors, 1996: Modeling of land-surface evaporation by four schemes and comparison with FIFE observations. *J. Geophys. Res.*, **101**, 7251–7268, <https://doi.org/10.1029/95JD02165>.
- Chen, M., P. Xie, and J. E. Janowiak, 2002: Global land precipitation: A 50-yr monthly analysis based on gauge observations. *J. Hydrometeor.*, **3**, 249–266, [https://doi.org/10.1175/1525-7541\(2002\)003<0249:GLPAYM>2.0.CO;2](https://doi.org/10.1175/1525-7541(2002)003<0249:GLPAYM>2.0.CO;2).
- Dee, D. P., and Coauthors, 2011: The ERA-Interim reanalysis: Configuration and performance of the data assimilation system. *Quart. J. Roy. Meteor. Soc.*, **137**, 553–597, <https://doi.org/10.1002/qj.828>.
- Diasso, U., and B. J. Abiodun, 2017: Drought modes in West Africa and how well CORDEX RCMs simulate them. *Theor. Appl. Climatol.*, **128**, 223–240, <https://doi.org/10.1007/s00704-015-1705-6>.
- Dole, R. M. P., and Coauthors, 2011: Was there a basis for anticipating the 2010 Russian heat wave? *Geophys. Res. Lett.*, **38**, L06702, <https://doi.org/10.1029/2010GL046582>.
- Duerinck, H. M., R. J. van der Ent, N. C. van de Giesen, G. Schoups, V. Babovic, and P. J.-F. Yeh, 2016: Observed soil moisture–precipitation feedback in Illinois: A systematic analysis over different scales. *J. Hydrometeor.*, **17**, 1645–1660, <https://doi.org/10.1175/JHM-D-15-0032.1>.
- Entin, J. K., A. Robock, K. Y. Vinnikov, S. E. Hollinger, S. Liu, and A. Namkhai, 2000: Temporal and spatial scales of observed soil moisture variations in the extratropics. *J. Geophys. Res.*, **105**, 11 865–11 877, <https://doi.org/10.1029/2000JD900051>.
- Fischer, E. M., S. I. Seneviratne, D. Lüthi, and C. Schär, 2007a: Contribution of land–atmosphere coupling to recent European summer heat waves. *Geophys. Res. Lett.*, **34**, L06707, <https://doi.org/10.1029/2006GL029068>.
- , —, P. L. Vidale, D. Lüthi, and C. Schär, 2007b: Soil moisture–atmosphere interactions during the 2003 European summer heat wave. *J. Climate*, **20**, 5081–5099, <https://doi.org/10.1175/JCLI4288.1>.
- Gochis, D., W. Shuttleworth, and Z. L. Yang, 2002: Sensitivity of the modeled North American monsoon regional climate to convective parameterization. *Mon. Wea. Rev.*, **130**, 1282–1298, [https://doi.org/10.1175/1520-0493\(2002\)130<1282:SOTMNA>2.0.CO;2](https://doi.org/10.1175/1520-0493(2002)130<1282:SOTMNA>2.0.CO;2).
- Grell, G. A., and D. Dévényi, 2002: A generalized approach to parameterizing convection combining ensemble and data assimilation techniques. *Geophys. Res. Lett.*, **29**, 1693, <https://doi.org/10.1029/2002GL015311>.
- , and S. R. Freitas, 2014: A scale and aerosol aware stochastic convective parameterization for weather and air quality modeling. *Atmos. Chem. Phys.*, **14**, 5233–5250, <https://doi.org/10.5194/acp-14-5233-2014>.
- Han, J., and H. L. Pan, 2011: Revision of convection and vertical diffusion schemes in the NCEP Global Forecast System. *Wea. Forecasting*, **26**, 520–533, <https://doi.org/10.1175/WAF-D-10-05038.1>.
- Han, T., H. Chen, and H. Wang, 2015: Recent changes in summer precipitation in Northeast China and the background circulation. *Int. J. Climatol.*, **35**, 4210–4219, <https://doi.org/10.1002/joc.4280>.
- , H. Wang, and J. Sun, 2017: Strengthened relationship between eastern ENSO and summer precipitation over northeastern China. *J. Climate*, **30**, 4497–4512, <https://doi.org/10.1175/JCLI-D-16-0551.1>.
- Hirschi, M., and Coauthors, 2011: Observational evidence for soil moisture impact on hot extremes in southeastern Europe. *Nat. Geosci.*, **4**, 17–21, <https://doi.org/10.1038/ngeo1032>.
- Hong, S. Y., Y. Noh, and J. Dudhia, 2006a: A new vertical diffusion package with an explicit treatment of entrainment processes. *Mon. Wea. Rev.*, **134**, 2318–2341, <https://doi.org/10.1175/MWR3199.1>.
- , J. H. Kim, J. O. Lim, and J. Dudhia, 2006b: The WRF single moment microphysics scheme (WSM). *J. Korean Meteor. Soc.*, **42**, 129–151.
- Iacono, M. J., J. S. Delamere, E. J. Mlawer, M. W. Shephard, S. A. Clough, and W. D. Collins, 2008: Radiative forcing by long-lived greenhouse gases: Calculations with the AER radiative transfer models. *J. Geophys. Res.*, **113**, D13103, <https://doi.org/10.1029/2008JD009944>.
- Jankov, I., W. A. Gallus Jr., M. Segal, B. Shaw, and S. E. Koch, 2005: The impact of different WRF model physical parameterizations and their interactions on warm season MCS rain. *Wea. Forecasting*, **20**, 1048–1060, <https://doi.org/10.1175/WAF888.1>.
- Kain, J. S., 2004: The Kain-Fritsch convective parameterization: An update. *J. Appl. Meteor.*, **43**, 170–181, [https://doi.org/10.1175/1520-0450\(2004\)043<0170:TKCPAU>2.0.CO;2](https://doi.org/10.1175/1520-0450(2004)043<0170:TKCPAU>2.0.CO;2).
- Koster, R. D., and Coauthors, 2004: Regions of strong coupling between soil moisture and precipitation. *Science*, **305**, 1138–1140, <https://doi.org/10.1126/science.1100217>.
- , Y. Chang, H. Wang, and S. Schubert, 2016: Impacts of local soil moisture anomalies on the atmospheric circulation and on remote surface meteorological fields during boreal summer: A comprehensive analysis over North America. *J. Climate*, **29**, 7345–7364, <https://doi.org/10.1175/JCLI-D-16-0192.1>.
- Lau, W. K. M., and K.-M. Kim, 2012: The 2010 Pakistan flood and Russian heat wave: Teleconnection of hydrometeorological extremes. *J. Hydrometeor.*, **13**, 392–403, <https://doi.org/10.1175/JHM-D-11-016.1>.
- Li, H., H. Chen, H. Wang, J. Sun, and J. Ma, 2018: Can Barents Sea ice decline in spring enhance summer hot drought events over northeastern China? *J. Climate*, **31**, 4705–4725, <https://doi.org/10.1175/JCLI-D-17-0429.1>.
- Li, K., J. Zhang, K. Yang, and L. Wu, 2019: The role of soil moisture feedbacks in future summer temperature change over East Asia. *J. Geophys. Res. Atmos.*, **124**, 12 034–12 056, <https://doi.org/10.1029/2018JD029670>.
- Li, W., W. Guo, Y. Xue, C. Fu, and B. Qiu, 2015: Sensitivity of a regional climate model to land surface parameterization schemes for East Asian summer monsoon simulation. *Climate Dyn.*, **47**, 2293–2308, <https://doi.org/10.1007/s00382-015-2964-8>.
- Li, X., W. Zhou, and Y. D. Chen, 2015: Assessment of regional drought trend and risk over China: A drought climate division perspective. *J. Climate*, **28**, 7025–7037, <https://doi.org/10.1175/JCLI-D-14-00403.1>.

- Liang, M., and X. Yuan, 2021: Critical role of soil moisture memory in predicting 2012 central USA flash drought. *Front. Earth Sci.*, **9**, 615969, <https://doi.org/10.3389/feart.2021.615969>.
- Liang, X.-Z., and Coauthors, 2012: Regional climate—Weather Research and Forecasting Model. *Bull. Amer. Meteor. Soc.*, **93**, 1363–1387, <https://doi.org/10.1175/BAMS-D-11-00180.1>.
- Lu, J., T. Feng, J. Li, Z. Cai, X. Xu, L. Li, and J. Li, 2019: Impact of assimilating Himawari-8-derived layered precipitable water with varying cumulus and microphysics parameterization schemes on the simulation of Typhoon Hato. *J. Geophys. Res. Atmos.*, **124**, 3050–3071, <https://doi.org/10.1029/2018JD029364>.
- Miralles, D. G., A. J. Teuling, C. C. van Heerwaarden, and J. Vilà-Guerau de Arellano, 2014: Mega heatwave temperatures due to combined soil desiccation and atmospheric heat accumulation. *Nat. Geosci.*, **7**, 345–349, <https://doi.org/10.1038/ngeo2141>.
- , P. Gentile, S. I. Seneviratne, and A. J. Teuling, 2019: Land-atmospheric feedbacks during droughts and heatwaves: State of the science and current challenges. *Ann. N. Y. Acad. Sci.*, **1436**, 19–35, <https://doi.org/10.1111/nyas.13912>.
- PaiMazumder, D., and J. M. Done, 2016: Potential predictability sources of the 2012 U.S. drought in observations and a regional model ensemble. *J. Geophys. Res. Atmos.*, **121**, 12 581–12 592, <https://doi.org/10.1002/2016JD025322>.
- Powers, J. G., and Coauthors, 2017: The Weather Research and Forecasting (WRF) Model: Overview, system efforts, and future directions. *Bull. Amer. Meteor. Soc.*, **98**, 1717–1737, <https://doi.org/10.1175/BAMS-D-15-00308.1>.
- Ren, X., D. Yang, and X. Yang, 2015: Characteristics and mechanisms of the subseasonal eastward extension of the South Asian high. *J. Climate*, **28**, 6799–6822, <https://doi.org/10.1175/JCLI-D-14-00682.1>.
- Roundy, J. K., C. R. Ferguson, and E. F. Wood, 2013: Temporal variability of land–atmosphere coupling and its implications for drought over the Southeast United States. *J. Hydrometeor.*, **14**, 622–635, <https://doi.org/10.1175/JHM-D-12-090.1>.
- Saha, S., and Coauthors, 2014: The NCEP Climate Forecast System version 2. *J. Climate*, **27**, 2185–2208, <https://doi.org/10.1175/JCLI-D-12-00823.1>.
- Schubert, S. D., H. Wang, and M. Suarez, 2011: Warm season subseasonal variability and climate extremes in the Northern Hemisphere: The role of stationary Rossby waves. *J. Climate*, **24**, 4773–4792, <https://doi.org/10.1175/JCLI-D-10-05035.1>.
- , —, R. D. Koster, M. J. Suarez, and P. Ya. Groisman, 2014: Northern Eurasian heat waves and droughts. *J. Climate*, **27**, 3169–3207, <https://doi.org/10.1175/JCLI-D-13-00360.1>.
- Schumacher, D. L., and Coauthors, 2019: Amplification of mega-heatwaves through heat torrents fuelled by upwind drought. *Nat. Geosci.*, **12**, 712–717, <https://doi.org/10.1038/s41561-019-0431-6>.
- Small, R. J. O., S. P. D. Szeoke, and S. P. Xie, 2007: The Central American midsummer drought: Regional aspects and large-scale forcing. *J. Climate*, **20**, 4853–4873, <https://doi.org/10.1175/JCLI4261.1>.
- Sun, J., and H. Wang, 2006: Regional difference of summer air temperature in Northeast China and its relationship to atmospheric general circulation and sea surface temperature (in Chinese). *Chin. J. Geophys.*, **49**, 588–598, <https://doi.org/10.1002/cjg2.872>.
- , and —, 2012: Changes of the connection between the summer North Atlantic Oscillation and the East Asian summer rainfall. *J. Geophys. Res.*, **117**, D08110, <https://doi.org/10.1029/2012JD017482>.
- Teuling, A. J., and Coauthors, 2013: Evapotranspiration amplifies European summer drought. *Geophys. Res. Lett.*, **40**, 2071–2075, <https://doi.org/10.1002/grl.50495>.
- Tiedtke, M., 1989: A comprehensive mass flux scheme for cumulus parameterization in large-scale models. *Mon. Wea. Rev.*, **117**, 1779–1800, [https://doi.org/10.1175/1520-0493\(1989\)117<1779:ACMFSF>2.0.CO;2](https://doi.org/10.1175/1520-0493(1989)117<1779:ACMFSF>2.0.CO;2).
- Vaidya, S. S., and S. S. Singh, 2000: Applying the Betts–Miller–Janjic scheme of convection in prediction of the Indian monsoon. *Wea. Forecasting*, **15**, 349–356, [https://doi.org/10.1175/1520-0434\(2000\)015<0349:ATBMJS>2.0.CO;2](https://doi.org/10.1175/1520-0434(2000)015<0349:ATBMJS>2.0.CO;2).
- Wang, Hailan, S. D. Schubert, R. D. Koster, and Y. Chang, 2019: Phase locking of the boreal summer atmospheric response to dry land surface anomalies in the Northern Hemisphere. *J. Climate*, **32**, 1081–1099, <https://doi.org/10.1175/JCLI-D-18-0240.1>.
- Wang, Huijun, and S. He, 2015: The North China/northeastern Asia severe summer drought in 2014. *J. Climate*, **28**, 6667–6681, <https://doi.org/10.1175/JCLI-D-15-0202.1>.
- Wang, S., X. Yuan, and R. Wu, 2019: Attribution of the persistent spring–summer hot and dry extremes over Northeast China in 2017. *Bull. Amer. Meteor. Soc.*, **100**, S85–S89, <https://doi.org/10.1175/BAMS-D-18-0120.1>.
- Wang, Z. Q., A. M. Duan, and G. X. Wu, 2014: Impacts of boundary layer parameterization schemes and air–sea coupling on WRF simulation of the East Asian summer monsoon. *Sci. China Earth Sci.*, **44**, 1480–1493, <https://doi.org/10.1007/s11430-013-4801-4>.
- Watanabe, M., and F.-F. Jin, 2003: A moist linear baroclinic model: Coupled dynamical–convective response to El Niño. *J. Climate*, **16**, 1121–1139, [https://doi.org/10.1175/1520-0442\(2003\)16<1121:AMLBMC>2.0.CO;2](https://doi.org/10.1175/1520-0442(2003)16<1121:AMLBMC>2.0.CO;2).
- Xue, Y., R. Vasic, Z. Janjić, Y. M. Liu, and P. C. Chu, 2012: The impact of spring subsurface soil temperature anomaly in the western U.S. on North American summer precipitation: A case study using regional climate model downscaling. *J. Geophys. Res.*, **117**, D11103, <https://doi.org/10.1029/2012JD017692>.
- , and Coauthors, 2016: Spring land temperature anomalies in northwestern US and the summer drought over Southern Plains and adjacent areas. *Environ. Res. Lett.*, **11**, 044018, <https://doi.org/10.1088/1748-9326/11/5/059502>.
- , and Coauthors, 2018: Spring land surface and subsurface temperature anomalies and subsequent downstream late spring–summer droughts/floods in North America and East Asia. *J. Geophys. Res. Atmos.*, **123**, 5001–5019, <https://doi.org/10.1029/2017JD028246>.
- Yanai, M., and T. Tomita, 1998: Seasonal and interannual variability of atmospheric heat sources and moisture sinks as determined from NCEP–NCAR reanalysis. *J. Climate*, **11**, 463–482, [https://doi.org/10.1175/1520-0442\(1998\)011<0463:SAIVOA>2.0.CO;2](https://doi.org/10.1175/1520-0442(1998)011<0463:SAIVOA>2.0.CO;2).
- Yu, M., Q. Li, M. J. Hayes, M. D. Svoboda, and R. R. Heim, 2014: Are droughts becoming more frequent or severe in China based on the standardized precipitation evapotranspiration index: 1951–2010? *Int. J. Climatol.*, **34**, 545–558, <https://doi.org/10.1002/joc.3701>.
- Yuan, X., and E. F. Wood, 2013: Multimodel seasonal forecasting of global drought onset. *Geophys. Res. Lett.*, **40**, 4900–4905, <https://doi.org/10.1002/grl.50949>.
- , X. Z. Liang, and E. F. Wood, 2012: WRF ensemble downscaling seasonal forecasts of China winter precipitation during 1982–2008. *Climate Dyn.*, **39**, 2041–2058, <https://doi.org/10.1007/s00382-011-1241-8>.
- , L. Wang, P. Wu, P. Ji, J. Sheffield, and M. Zhang, 2019: Anthropogenic shift towards higher risk of flash drought over China. *Nat. Commun.*, **10**, 4661, <https://doi.org/10.1038/s41467-019-12692-7>.

- , F. Ma, H. Li, and S. Chen, 2020: A review on multi-scale drought processes and prediction under global change (in Chinese). *Trans. Atmos. Sci.*, **43**, 225–237.
- Zaitchik, B. F., J. A. Santanello, S. V. Kumar, and C. D. Peters-Lidard, 2013: Representation of soil moisture feedbacks during drought in NASA Unified WRF (NU-WRF). *J. Hydrometeor.*, **14**, 360–367, <https://doi.org/10.1175/JHM-D-12-069.1>.
- Zeng, D., and X. Yuan, 2018: Multi-scale land–atmosphere coupling and its application in assessing subseasonal forecasts over East Asia. *J. Hydrometeor.*, **19**, 745–760, <https://doi.org/10.1175/JHM-D-17-0215.1>.
- , —, and J. K. Roundy, 2019: Effect of teleconnected land–atmosphere coupling on Northeast China persistent drought in spring–summer of 2017. *J. Climate*, **32**, 7403–7420, <https://doi.org/10.1175/JCLI-D-19-0175.1>.
- Zhai, J., B. Su, V. Krysanova, T. Vetter, C. Gao, and T. Jiang, 2010: Spatial variation and trends in PDSI and SPI indices and their relation to streamflow in 10 large regions of China. *J. Climate*, **23**, 649–663, <https://doi.org/10.1175/2009JCLI2968.1>.
- Zhang, C., and Y. Wang, 2017: Projected future changes of tropical cyclone activity over the western North and South Pacific in a 20-km-mesh regional climate model. *J. Climate*, **30**, 5923–5941, <https://doi.org/10.1175/JCLI-D-16-0597.1>.
- Zhang, L., and T. Zhou, 2015: Drought over East Asia: A review. *J. Climate*, **28**, 3375–3399, <https://doi.org/10.1175/JCLI-D-14-00259.1>.
- Zhang, R., and Z. Zuo, 2011: Impact of spring soil moisture on surface energy balance and summer monsoon circulation over East Asia and precipitation in East China. *J. Climate*, **24**, 3309–3322, <https://doi.org/10.1175/2011JCLI4084.1>.
- Zheng, Y., K. Alapaty, J. A. Herwehe, A. D. Del Genio, and D. Niyogi, 2016: Improving high-resolution weather forecasts using the Weather Research and Forecasting (WRF) model with an updated Kain–Fritsch scheme. *Mon. Wea. Rev.*, **144**, 833–860, <https://doi.org/10.1175/MWR-D-15-0005.1>.
- Zhong, Z., Y. Hu, J. Min, and H. Xu, 2007: Numerical experiments on the spin-up time for seasonal-scale regional climate modeling. *J. Meteor. Res.*, **21**, 409–419.
- Zhou, S., and Coauthors, 2019: Land–atmosphere feedbacks exacerbate concurrent soil drought and atmospheric aridity. *Proc. Natl. Acad. Sci. USA*, **116**, 18 848–18 853, <https://doi.org/10.1073/pnas.1904955116>.